

See discussions, stats, and author profiles for this publication at: <https://www.researchgate.net/publication/49691228>

# Intrinsic Optical Properties of Vanadium Dioxide near the Insulator–Metal Transition

ARTICLE *in* NANO LETTERS · FEBRUARY 2011

Impact Factor: 13.59 · DOI: 10.1021/nl1032205 · Source: PubMed

CITATIONS

37

READS

28

8 AUTHORS, INCLUDING:



**Zhao Hao**

University of California, Berkeley

70 PUBLICATIONS 3,043 CITATIONS

SEE PROFILE



**Michael C Martin**

Lawrence Berkeley National Laboratory

194 PUBLICATIONS 5,981 CITATIONS

SEE PROFILE



**yi-ren Shen**

China Medical University (ROC)

249 PUBLICATIONS 10,562 CITATIONS

SEE PROFILE



**Jiong Wu**

Fudan University

375 PUBLICATIONS 9,087 CITATIONS

SEE PROFILE

# Intrinsic Optical Properties of Vanadium Dioxide near the Insulator–Metal Transition

Wei-Tao Liu,<sup>\*,†</sup> J. Cao,<sup>‡</sup> W. Fan,<sup>§</sup> Zhao Hao,<sup>||</sup> Michael C. Martin,<sup>⊥</sup> Y. R. Shen,<sup>†</sup> J. Wu,<sup>‡</sup> and F. Wang<sup>\*,†</sup>

<sup>†</sup>Department of Physics, University of California at Berkeley, Berkeley, California 94720, United States

<sup>‡</sup>Department of Material Science and Engineering, University of California at Berkeley, Berkeley, California 94720, United States

<sup>§</sup>Department of Thermal Science and Energy Engineering, University of Science and Technology of China, Hefei, China

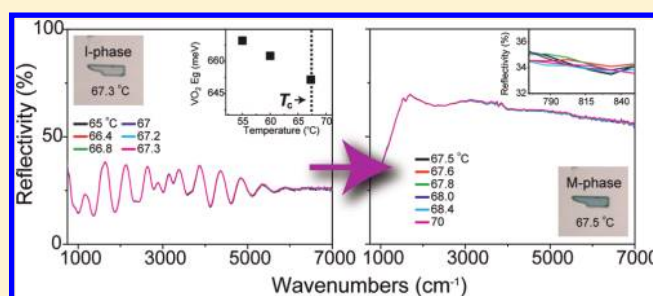
<sup>||</sup>Earth Sciences Division, Lawrence Berkeley National Laboratory, Berkeley, California 94720, United States

<sup>⊥</sup>Advanced Light Source Division, Lawrence Berkeley National Laboratory, Berkeley, California 94720, United States

**S** Supporting Information

**ABSTRACT:** We studied the insulator–metal transition (IMT) in single-domain, single crystalline vanadium dioxide (VO<sub>2</sub>) microbeams with infrared microspectroscopy. The unique nature of such samples allowed us to probe the intrinsic behavior of both insulating and metallic phases in the close vicinity of IMT, and investigate the IMT driven by either strain or temperature independently. We found that the VO<sub>2</sub> insulating band gap narrows rapidly upon heating, and the infrared response undergoes an abrupt transition at both strain- and temperature-induced IMT. The results are consistent with recent studies attributing the opening of VO<sub>2</sub> insulating band gap to a correlation-assisted Peierls transition.

**KEYWORDS:** Vanadium dioxide, insulator–metal transition, phase transition, infrared microspectroscopy, correlated electron nanomaterials



Transition metal oxides exhibit many fascinating phenomena, such as high-temperature superconductivity, colossal magnetoresistance, and insulator–metal transitions. In these oxides, competing states can often coexist and form nano- or microscale domains of different phases.<sup>1</sup> This inhomogeneity often obscures the intrinsic property of individual phases and makes it challenging to test theoretical models based on homogeneous systems.<sup>2,3</sup> One way to overcome this difficulty is to investigate nano- or microscale samples, which are smaller than the characteristic domain size and can remain single-domain during phase transitions.

Vanadium dioxide (VO<sub>2</sub>) is a typical example. It undergoes an insulator–metal transition (IMT) coupled with a structural transition when heated through  $\sim 68$  °C. Though the phenomenon has been known for decades,<sup>4</sup> its precise mechanism remains controversial: some studies attributed the opening of the insulating band gap to the Peierls dimerization,<sup>5,6</sup> while others suggested that Coulomb repulsion between localized vanadium 3d electrons is more important.<sup>7,8</sup> To resolve this controversy, the precise knowledge of VO<sub>2</sub> properties in the close vicinity of IMT is essential. However, many of previous studies used large-scale VO<sub>2</sub> samples with complicated domain structures near IMT,<sup>7,8</sup> which hampered direct measurements of individual phases. Recently, single-crystalline VO<sub>2</sub> micro- and

nanobeams have been synthesized with the vapor transport method.<sup>9,10</sup> They contain an extremely low level of defects and impurities for heterogeneous nucleations and can remain single-domain across the phase transition,<sup>9,11</sup> allowing us to probe intrinsic properties of individual phases in the close vicinity of IMT. Transport and Raman studies on VO<sub>2</sub> microbeams have yielded valuable information of phonons and carriers at the Fermi level,<sup>11,12</sup> yet there still lacks detailed investigation on the electronic structure, which shall help further elucidate the nature of the IMT.

In this paper, we report a study on the IMT in single-domain VO<sub>2</sub> microbeams using confocal Fourier-transform infrared (FTIR) microspectroscopy. Previous infrared studies on multi-domain VO<sub>2</sub> thin films found peculiar features near IMT such as a pseudogap centered at  $\sim 800$  cm<sup>-1</sup>,<sup>7,8</sup> yet complex analyses were required to extract information for individual phases. Now with single-domain samples, we can determine the property of each phase directly. In addition, the unique nature of single-domain microbeams allowed us to vary temperature and strain independently, and monitor the IMT happening in each case. In

**Received:** September 13, 2010

**Revised:** December 12, 2010

**Published:** December 17, 2010

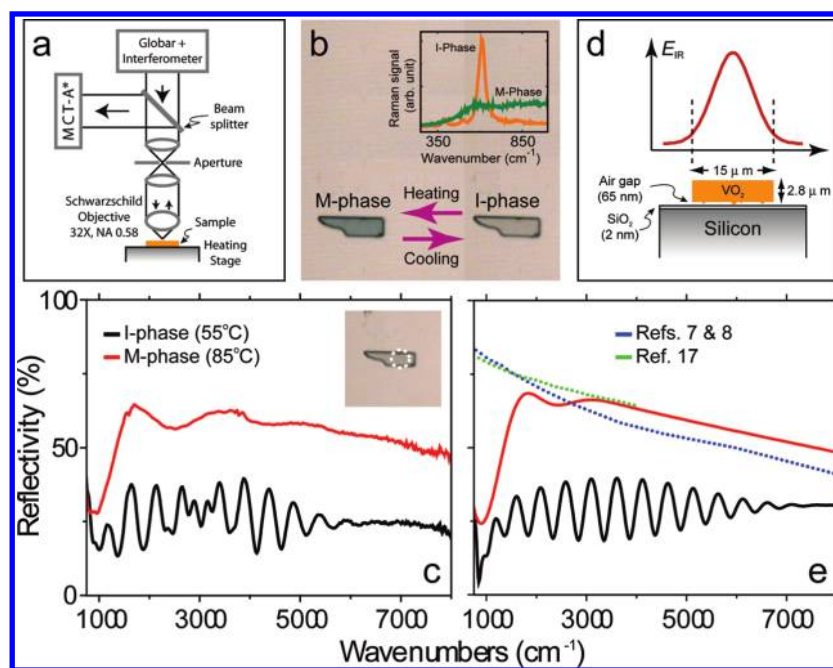


**Figure 1.** (a) Schematics of the experimental setup. (b) Visible-light microscopy image and Raman spectra (inset) of a single-domain  $\text{VO}_2$  microbeam in different phases. (c) Measured infrared reflectivity of the  $\text{VO}_2$  microbeam in different phases. Inset: Illumination area of the infrared light. (d) Geometries of the  $\text{VO}_2$  microbeam and infrared beam. (e) Calculated infrared reflectivity of the  $\text{VO}_2$  microbeam in different phases; dotted lines are infrared reflectivity from thin film  $\text{VO}_2$  samples in the pure M-phase with parameters in refs 7, 8, and 17.

the text, we will first describe our method for quantitative analysis of microbeam infrared spectra. On the basis of the spectra, we found that (1) upon heating, the insulating band gap energy reduces by  $\sim 1\text{--}1.5\text{ meV}/^\circ\text{C}$  to a finite value at IMT, and (2) the  $\text{VO}_2$  infrared response changes abruptly across IMT driven by either strain or temperature, with no transitional state resolvable in our spectral range. The observation agreed with a first-order structural transition, and the quick narrowing of the band gap toward IMT suggested the importance of carrier–carrier interaction. Overall, our results are in consent with recent recognitions that the correlation interaction adds to the effect of Peierls pairing in  $\text{VO}_2$ , and together they lead to the phase transition.<sup>13,14</sup>

The synthesis of single-crystalline  $\text{VO}_2$  microbeams was described elsewhere.<sup>9,10</sup> In our measurements, the microbeams were transferred to either a weakly interacting substrate (silicon with native oxide) to eliminate the strain or a bendable Kapton substrate for controlling the strain. In the latter case, the sample was fixed to the substrate using epoxy.<sup>15</sup> A Linkam FTIR 600 heating stage was used in measuring strain-free samples, and a homemade stage to apply strain with temperature regulated by a Lakeshore 331 controller. An accuracy of  $0.1^\circ\text{C}$  in the temperature was achieved in both cases. The infrared reflectivity spectra were taken with an FTIR spectrometer (Thermo Nicolet Nexus 870) combined with a confocal microscope (Nicolet Continuum XL) using a  $32\times$  Schwarzschild objective (numerical aperture 0.58), and the signal was collected with a liquid-nitrogen-cooled mercury cadmium telluride (MCT-A\*) detector (shown schematically in Figure 1a). The reflectivity from a flat gold film was used for normalization. All  $\text{VO}_2$  spectra were taken after the sample being stabilized under the given temperature or strain for about 5 min.

In our experiments, we identified different phases of  $\text{VO}_2$  microbeams from both their Raman spectra<sup>12</sup> and visible-light optical microscope images, showing different contrast in the

insulating (I) and metallic (M) phases.<sup>9,15</sup> Figure 1b shows the optical images and Raman spectra of a  $\sim 15\text{ }\mu\text{m}$  wide microbeam in its pure I and M phases, respectively. The corresponding infrared reflectivity spectra for the two phases are displayed in Figure 1c, with the illumination area marked schematically by the white circle (inset). Qualitatively, the electronic structure of  $\text{VO}_2$  in the I-phase is characterized by an energy gap,  $E_g \sim 670\text{ meV}$  ( $\sim 5400\text{ cm}^{-1}$ ), between the  $d_{||}$  and  $\pi^*$  bands of vanadium 3d electrons,<sup>16</sup> which causes strong optical absorption above  $E_g$ . Below  $E_g$ , the optical absorption of  $\text{VO}_2$  is weak,<sup>17</sup> and the interference between light reflected from sample top and bottom surfaces led to the periodic fringes seen in the I-phase spectrum. In the M-phase the  $\text{VO}_2$  optical response is dominated by that from free carriers<sup>7,8,17</sup> and shows high infrared reflectivity. Due to the diffraction of light, the infrared focal spot became larger than the  $\text{VO}_2$  microbeam at longer wavelength, so a smaller fraction of light was reflected from the sample and the overall reflectivity dropped.

To ensure that spectral features due to extrinsic factors (such as the shape of the sample) are separable from those due to  $\text{VO}_2$  intrinsic properties, we simulated the infrared spectra by taking into account geometries of both the microbeam and infrared focal spot. We considered a multilayer system including the  $15\text{ }\mu\text{m}$  wide,  $2.8\text{ }\mu\text{m}$  thick (measured with atomic force microscopy)  $\text{VO}_2$  microbeam, a native silicon dioxide layer  $\sim 2\text{ nm}$  thick, and the silicon substrate (Figure 1d). Since the microbeam was clamped tightly to a wafer during the growth, its bottom surface was slightly roughened. We included an effective air gap between  $\text{VO}_2$  and the substrate to account for that roughness. The normal incident infrared light was unpolarized, and we assumed a Gaussian field distribution across the focal spot (Figure 1d) that broadened with the wavelength ( $\lambda$ ). We then calculated the overall reflectivity by evaluating characteristic matrices<sup>18</sup> of all layers, using optical constants of  $\text{VO}_2$  extracted

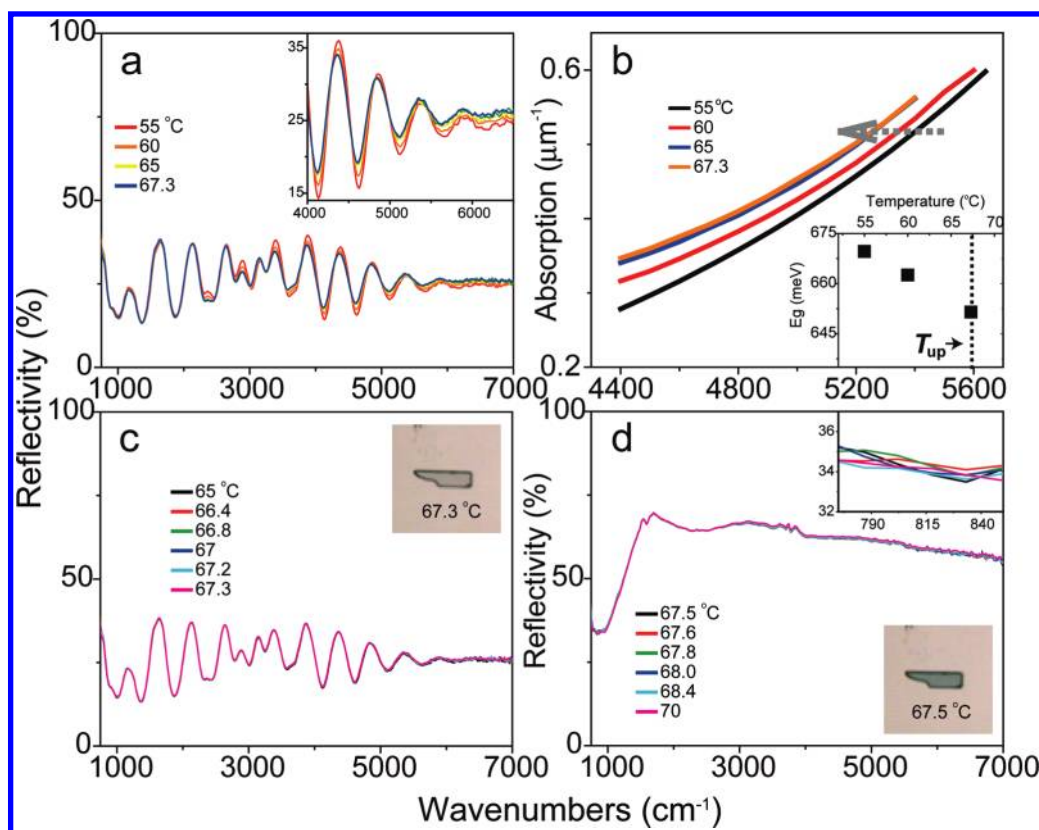


**Figure 2.** (a) Infrared reflectivity of a single-domain  $\text{VO}_2$  microbeam in the I-phase at different temperatures. Inset: Magnification of the spectra within  $4000\text{--}7000\text{ cm}^{-1}$ . (b) The deduced  $\text{VO}_2$  absorption coefficient at different temperatures. Inset: Temperature dependence of  $E_g$  near IMT. (c, d) Infrared reflectivity of the single-domain  $\text{VO}_2$  microbeam in I and M phases, respectively, near the transition temperature. Inset in (d) Magnification of the spectra within  $775\text{--}825\text{ cm}^{-1}$ .

from large-scale samples in pure phases.<sup>7,8,17</sup> Finally, we combined contributions from both the microbeam and adjacent silicon substrate to obtain the total reflectivity. Details of the calculation are provided in the Supporting Information.

By fitting to the contrast of fringes in the I-phase we determined the thickness of the air gap to be 65 nm. The best fit of the entire I-phase spectrum (Figure 1e) was then obtained with the full width at half-maximum of the infrared focal spot being  $\sim 1.2\text{--}1.6\lambda$ , which is reasonable for a Global source under the confocal setup.<sup>19,20</sup> With the same parameters, we could also obtain satisfactory fit of the M-phase spectrum (Figure 1e). The reflectivity drop at the longer wavelength was well reproduced. The deviation of our fits from measured spectra was likely due to nonideal infrared spot and sample geometries. Overall, the result confirmed that optical parameters of large-scale  $\text{VO}_2$  samples are readily applicable to  $\text{VO}_2$  microbeams. It also showed that we could distinguish spectral features due to  $\text{VO}_2$  intrinsic properties from those due to extrinsic factors, which enabled our further analyses.

Having understood the microbeam infrared spectra, we now focus on spectral features related to the IMT. Upon IMT, the  $\text{VO}_2$  lattice contracts by  $\sim 1\%$  along the tetragonal  $c$  axis and expands by 0.6 and 0.4% along the other two principle axes.<sup>15</sup> In multidomain samples, the inhomogeneous volume change of neighboring domains upon heating/cooling causes an internal strain. Hence effects of temperature and strain are always entangled, which complicates experimental studies. While with single-domain samples, the two parameters become separable.

We first studied the temperature-driven IMT at zero strain. This was achieved by transferring the  $\text{VO}_2$  microbeam to a weakly coupled beam–substrate interface, on which the sample could slip freely and experienced effectively no strain.<sup>9</sup> Due to the high crystal uniformity, the metallic phase could be supercooled below the phase boundary, and the microbeam exhibited two distinct transition temperatures upon heating and cooling,<sup>9,11</sup> named as  $T_{\text{up}}$  and  $T_{\text{down}}$ , respectively. Multidomain samples always show a gradual change in optical and electric properties over a wide range of temperatures,<sup>7,8</sup> making it difficult to determine the transition point accurately. In contrast, both  $T_{\text{up}}$  and  $T_{\text{down}}$  of single-domain samples can be determined with an accuracy of  $\pm 0.1\text{ }^\circ\text{C}$  and are very well reproducible during multiple heating-and-cooling cycles. For the sample shown in Figure 1, we had  $T_{\text{up}}$  and  $T_{\text{down}}$  being  $67.4$  and  $64.0\text{ }^\circ\text{C}$ , respectively. Below we will only discuss spectra recorded upon heating because the same results were obtained upon cooling.

In the I-phase, four spectra taken at different temperatures are shown in Figure 2a. The spectra overlapped perfectly below  $\sim 2000\text{ cm}^{-1}$ , while at higher frequencies the contrast of interference fringes gradually decreased upon heating. The insulating  $\text{VO}_2$  can exhibit two different structures, the monoclinic  $M_1$  and  $M_2$  phases, respectively, but the  $M_2$  phase only exists under large uniaxial stress or with high doping<sup>21,22</sup> and was negligible in our strain-free samples. The observed change in optical properties came from the  $M_1$  phase. On the basis of our analysis above, such change can be explained by an increasing optical absorption right below the low-temperature  $E_g$  or effectively a reduction of  $E_g$  at



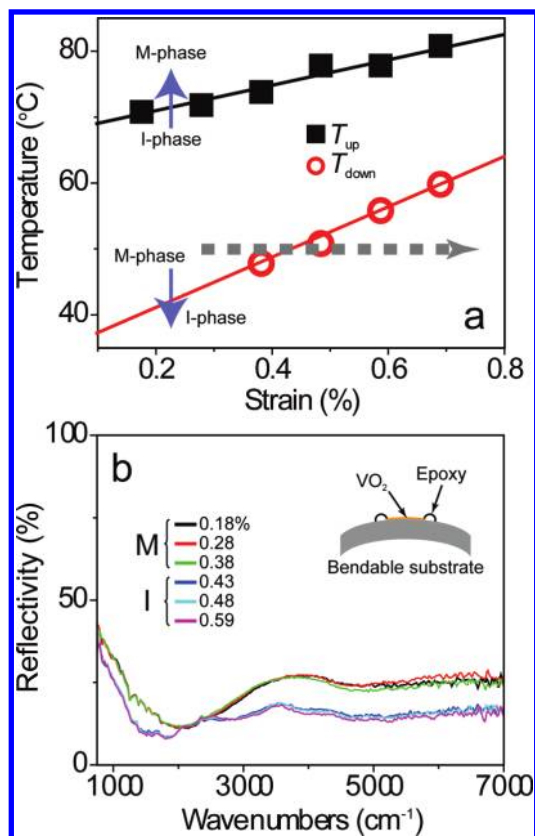


**Figure 3.** (a) Phase diagram of a single-domain VO<sub>2</sub> microbeam under strain and temperature variations. (b) Infrared reflectivity of the VO<sub>2</sub> beam in the vicinity of strain-induced IMT at 50 °C. Inset: A schematic of the bendable Kapton device.

elevated temperatures. Previous infrared studies on bulk VO<sub>2</sub> samples observed a similar trend,<sup>23</sup> yet they were limited by the sample inhomogeneity and could not access the pure I-phase at very close to IMT. With the single-domain microbeam we can now monitor the infrared spectrum continuously to 0.1 °C below  $T_{up}$ . Quantitatively, we deduced the optical absorption coefficient at different temperatures, as plotted in Figure 2b (details are in the Supporting Information). Following the convention in ref 23, we used the infrared frequency corresponding to a constant absorption coefficient to represent  $E_g$  and obtained its temperature dependence assuming  $E_g = 670$  meV at 55 °C (inset in Figure 2b). We found that  $E_g$  decreases by  $\sim 1.5$  meV/°C from 55 to 67.3 °C, comparable to results of previous infrared and photoemission studies on bulk samples, being about  $\sim 1$  meV/°C from  $\sim 0$  to 60 °C.<sup>23,24</sup> It is also clearly seen that  $E_g$  remained a finite value at the IMT, which is consistent with the nature of a first-order structural transition.

Now we focus on infrared spectra in the close vicinity of IMT. Panels c and d of Figure 2 display spectra taken within about  $\pm 2$  °C around  $T_{up}$ . The I-phase spectra overlapped almost perfectly (Figure 2c), so did the M-phase spectra (Figure 2d), with an abrupt transition between the two phases within  $\pm 0.1$  °C around  $T_{up}$ . This result is anticipated for a first-order structural transition but is in contrast to the behavior observed in multidomain thin film samples,<sup>7,8</sup> where the optical conductivity of metallic domains evolves gradually within a few degrees above the transition temperature due to a pseudogap centered at  $\sim 800$  cm<sup>-1</sup>. If the same pseudogap existed in our VO<sub>2</sub> microbeam, we then

expect a reflectivity change of  $\sim 5\%$  within 2 °C above  $T_{up}$  as estimated from the data in refs 7 and 8. However, our measured spectra had an uncertainty less than 1%, and within this uncertainty all M-phase spectra were identical (inset of Figure 2d). Therefore, we conclude that unlike in multidomain thin films, the infrared response from single-domain VO<sub>2</sub> microbeams undergoes an much more abrupt transition across IMT, with properties of free carriers, such as the plasma frequency and scattering rate, remaining unchanged right above the transition temperature.

We now study the strain-induced IMT at a fixed temperature. Due to their high crystal uniformity, narrow VO<sub>2</sub> microbeams can be artificially stressed under extraordinarily large strain without plastic deformation or fracture.<sup>11,15,22</sup> The schematic view of a VO<sub>2</sub> microbeam on a bendable Kapton substrate is shown in the inset of Figure 3b. Once fixed tightly to the substrate surface, the microbeam could be strained by bending the substrate. In our measurement, we used a sample that remained single-domain under all applied strains and temperatures. We first mapped out the phase diagram of this microbeam by recording  $T_{up}$  and  $T_{down}$  at each given strain (Figure 3a). Both  $T_{up}$  and  $T_{down}$  varied about linearly with the strain as shown in ref 15. We then brought the sample to the M-phase, fixed the temperature at 50 °C, and varied the strain along the trajectory indicated by the dashed gray line. Spectra recorded under various strains are shown in Figure 3b. Within our detection uncertainty ( $<2\%$ ), there was no observable spectral change in each phase below  $\sim 2000$  cm<sup>-1</sup>, and again a precipitous transition occurred across the IMT. The result demonstrated that the VO<sub>2</sub> infrared response undergoes an abrupt transition upon IMT, regardless of the driving force being strain or temperature. This is consistent with recent transport measurements that unified effects of strain and temperature variations on the IMT.<sup>11</sup>

All our results above showed an abrupt first-order transition at VO<sub>2</sub> IMT driven by either temperature or strain; besides, we obtained quantitative information of  $E_g$  near the IMT, which reduces at a rate  $\sim 1\text{--}1.5$  meV/°C upon heating. In semiconductors, there are two major mechanisms that could renormalize the band gap energy. One is due to lattice effects such as the thermal expansion,<sup>25</sup> while the consequent energy gap reduction rate is usually less than that in VO<sub>2</sub>. For example, at above 300 K, the linear expansion coefficient of the I-phase VO<sub>2</sub><sup>26</sup> is similar to that of Ge,<sup>27</sup> but the band gap narrows by only  $\sim 0.4$  meV/°C in the latter.<sup>23</sup> The other mechanism is due to the carrier–carrier interaction, including contributions from both the exchange and correlation energies. Magnitude of the corresponding band gap narrowing increases with the carrier density.<sup>28</sup> To estimate that value for VO<sub>2</sub>, we first calculated its carrier density versus the temperature, with an activation energy  $\sim 0.3$  eV<sup>11</sup> and a carrier density  $\sim 5 \times 10^{18}$  cm<sup>-3</sup> at the IMT. The latter was evaluated from a critical resistivity  $\sim 12$  Ω cm<sup>11</sup> and mobility  $\sim 0.11$  cm<sup>2</sup>/(V s).<sup>29,30</sup> Assuming similar parameters for VO<sub>2</sub> to those for heavily doped Si, Ge, and GaAs,<sup>27</sup> we would find that the carrier–carrier interaction could also cause a few tenths of meV/°C reduction in  $E_g$ . The result basically suggests that the band gap change in VO<sub>2</sub> and conventional semiconductors are due to the same types of fundamental interaction, but quantitatively, the contribution from carrier–carrier interaction can be more important in VO<sub>2</sub> than in others. It is in accordance with recent theoretical studies that attributed the VO<sub>2</sub> IMT to a correlation-assisted Peierls transition,<sup>13,14</sup> which also agreed with Mott's initial conjecture.<sup>31</sup> Further theoretical and experimental investigations are needed to accurately evaluate how

carrier–lattice and carrier–carrier interactions contribute to the VO<sub>2</sub> band gap renormalization. The latter, for example, could be accurately monitored by doping VO<sub>2</sub> via electrical gating.

To conclude, we have studied the IMT in single-domain, single crystalline VO<sub>2</sub> microbeams with the infrared microspectroscopy. We did quantitative analysis of the microbeam infrared spectra and distinguished features due to VO<sub>2</sub> intrinsic properties. In contrast to multidomain samples, single-domain samples exhibited abrupt transitions across the IMT driven by either strain or temperature, with no transitional state resolvable in our spectral range. We also found that the VO<sub>2</sub> insulating band gap energy reduces quickly upon heating to a finite value at the IMT. The results suggested a first-order structural transition strongly affected by the carrier–carrier interaction. Future studies in the lower frequency region shall provide more understanding of the near-threshold behavior of the Fermi surface. More generally, our study demonstrated that with nano- and microscale samples smaller than the characteristic domain size, we could reliably obtain intrinsic properties of individual phases in complex oxides. Revisiting those systems with single-domain samples shall shed new light on their precise physical nature.

## ■ ASSOCIATED CONTENT

**S Supporting Information.** Details of calculations in the paper. This material is available free of charge via the Internet at <http://pubs.acs.org>.

## ■ AUTHOR INFORMATION

### Corresponding Author

\*E-mail: [wliu@uclink.berkeley.edu](mailto:wliu@uclink.berkeley.edu) and [fengwang76@berkeley.edu](mailto:fengwang76@berkeley.edu).

## ■ ACKNOWLEDGMENT

This work was supported by the Department of Energy Early Career Award DE-SC0003949 and by the Office of Basic Energy Sciences under Contract No. DE-AC02-05CH11231 (Advanced Light Source). The material synthesis was supported and The National Science Foundation (NSF) under Grant No. EEC-0832819. The Advanced Light Source is supported by the Director, Office of Science, Office of Basic Energy Sciences, of the U.S. Department of Energy under Contract No. DE-AC02-05CH11231.

## ■ REFERENCES

- (1) Dagotto, E. *Science* **2005**, *309*, 257–262.
- (2) Dagotto, E.; Hotta, T.; Moreo, A. *Phys. Rep.* **2001**, *344*, 1–153.
- (3) Dagotto, E. *Nanoscale Phase Separation and Colossal Magnetoresistance*; Springer-Verlag: Berlin, 2002.
- (4) Morin, F. J. *Phys. Rev. Lett.* **1959**, *3*, 34–36.
- (5) Wentzcovitch, R. M.; Schulz, W. W.; Allen, P. B. *Phys. Rev. Lett.* **1994**, *72*, 3389–3392.
- (6) Booth, J. M.; Casey, P. S. *Phys. Rev. Lett.* **2009**, *103*, No. 086402.
- (7) Qazilbash, M. M.; et al. *Science* **2007**, *318*, 1750–1753.
- (8) Qazilbash, M. M.; et al. *Phys. Rev. B* **2009**, *79*, No. 075107.
- (9) Wu, J. Q.; Gu, Q.; Guiton, B. S.; de Leon, N. P.; Ouyang, L.; Park, H. *Nano Lett.* **2006**, *6*, 2313–2317.
- (10) Guiton, B. S.; Gu, Q.; Prieto, A. L.; Gudiksen, M. S.; Park, H. *J. Am. Chem. Soc.* **2005**, *127*, 498–499.
- (11) Wei, J.; Wang, Z.; Chen, W.; Cobden, D. H. *Nat. Nanotechnol.* **2009**, *4*, 420–424.
- (12) (a) Jones, A. C.; Berweger, S.; Wei, J.; Cobden, D. H.; Raschke, M. B. *Nano Lett.* **2010**, *10*, 1574–1581. (b) Zhang, S.; Chou, J. Y.; Lauhon, L. J. *Nano Lett.* **2009**, *9*, 4527–4532.
- (13) Biermann, S.; Poteryaev, A.; Lichtenstein, A. I.; Georges, A. *Phys. Rev. Lett.* **2005**, *94*, No. 026404.
- (14) Tomczak, J. M.; Aryasetiawan, F.; Biermann, S. *Phys. Rev. B* **2008**, *78*, No. 115103.
- (15) Cao, J.; et al. *Nat. Nanotechnol.* **2009**, *4*, 732–737.
- (16) Rini, M.; et al. *Appl. Phys. Lett.* **2008**, *92*, No. 181904.
- (17) Barker, A. S., Jr.; Verleur, H. W.; Guggenheim, H. J. *Phys. Rev. Lett.* **1966**, *17*, 1286–1289.
- (18) Abdulhalim, I. J. *Opt. A* **1999**, *1*, 655–661.
- (19) Hummel, H. J. *Practical Guide to Infrared Microspectroscopy*; Marcel Dekker: New York, 1995; Chapter 1.
- (20) Levenson, E.; Lerch, P.; Martin, M. C. *Infrared Phys. Technol.* **2008**, *51*, 413–416.
- (21) Eyert, V. *Ann. Phys.* **2002**, *15*, 650–702.
- (22) Cao, J.; Gu, Y.; Fan, W.; Chen, L. Q.; Ogletree, D. F.; Chen, K.; Tamura, N.; Kunz, M.; Barrett, C.; Seidel, J.; Wu, J. *Nano Lett.* **2010**, *10*, 2667–2673.
- (23) Ladd, L. A.; Paul, W. *Solid State Commun.* **1969**, *7*, 425–428.
- (24) Okazaki, K.; Fujimori, A.; Onoda, M. *J. Phys. Soc. Jpn.* **2002**, *71*, 822–825.
- (25) Ünlü, H. *Solid-State Electron.* **1992**, *35*, 1343–1352.
- (26) Kucharczyk, D.; Niklewski, T. *J. Appl. Crystallogr.* **1979**, *12*, 370–373.
- (27) Novikova, S. I. *Sov. Phys. Solid State* **1969**, *2*, 37–38.
- (28) Jain, S. C.; Roulston, D. J. *Solid-State Electron.* **1991**, *34*, 453–465.
- (29) Ruzmetov, D.; et al. *Phys. Rev. B* **2009**, *79*, No. 153107.
- (30) Cao, J.; et al. *Phys. Rev. B* **2010**, *82*, No. 241101(R).
- (31) Zylbersztejn, A.; Mott, N. F. *Phys. Rev. B* **1975**, *11*, 4383–4395.

## Supporting Information

# Intrinsic Optical Properties of Vanadium Dioxide Near the Insulator-Metal-Transition

*Wei-Tao Liu<sup>1\*</sup>, J. Cao<sup>2</sup>, W. Fan<sup>2</sup>, Zhao Hao<sup>3</sup>, Michael C. Martin<sup>4</sup>, Y. R. Shen<sup>1</sup>, J. Wu<sup>2</sup>, and  
F. Wang<sup>1\*</sup>*

<sup>1</sup>Department of Physics, University of California at Berkeley, Berkeley, CA 04720, USA,

<sup>2</sup>Department of Material Science and Engineering, University of California at Berkeley,  
Berkeley, CA 04720, USA,

<sup>3</sup>Earth Sciences Division, Lawrence Berkeley National Laboratory, Berkeley, CA 94720,  
USA,

<sup>4</sup>Advanced Light Source Division, Lawrence Berkeley National Laboratory, Berkeley, CA  
94720, USA.

### 1. Refractive indices of materials:

a) VO<sub>2</sub> in I-phase:

For VO<sub>2</sub> in the I-phase, we used the classical oscillator expression:<sup>S1</sup>

---

\*E-mail: [wliu@uclink.berkeley.edu](mailto:wliu@uclink.berkeley.edu); [fengwang76@berkeley.edu](mailto:fengwang76@berkeley.edu)

$$n^2(\omega) - \kappa^2(\omega) = \varepsilon_\infty + \sum_j \frac{4\pi\rho_j\omega_j^2(\omega_j^2 - \omega^2)}{(\omega_j^2 - \omega^2)^2 + \gamma_j^2\omega_j^2\omega^2},$$

$$2n(\omega)\kappa(\omega) = \sum_j \frac{4\pi\rho_j\omega_j^3\gamma_j\omega}{(\omega_j^2 - \omega^2)^2 + \gamma_j^2\omega_j^2\omega^2},$$

to calculate its complex refractive index,  $\tilde{n} = n + i\kappa$ , with  $\omega$  being the infrared frequency, and  $\omega_j$ ,  $4\pi\rho_j$ ,  $\gamma_j$  being the resonant frequency, amplitude, and damping coefficient of the  $j^{\text{th}}$  resonance mode, respectively. Corresponding values of  $\omega_j$ ,  $4\pi\rho_j$ ,  $\gamma_j$  are listed in Table I of Ref. 17.

b) VO<sub>2</sub> in M-phase:

For VO<sub>2</sub> in the M-phase, we obtained  $\tilde{n}$  from the relative dielectric constant  $\tilde{\varepsilon}_r = \tilde{n}^2$  using the Drude model, which gives:<sup>S2</sup>

$$\varepsilon_r'(\omega) = 1 - \frac{\omega_p^2\tau^2}{1 + \omega_p^2\tau^2},$$

$$\varepsilon_r''(\omega) = \frac{\omega_p^2\tau}{\omega(1 + \omega_p^2\tau^2)},$$

with  $\varepsilon_r' + i\varepsilon_r'' = \tilde{\varepsilon}_r$ , and  $\omega_p$ ,  $\tau$  being the plasma frequency and scattering time, respectively. Corresponding values of  $\omega_p$  and  $\tau$  are provided in Ref. 7 for M-phase VO<sub>2</sub> at 360 K.

c) Si and SiO<sub>2</sub>:

Refractive indices of Si and SiO<sub>2</sub> are obtained from Ref. S3.

## 2. Characteristic matrix method:



The characteristic matrix method is commonly used to analyze the propagation of light through a layered system.<sup>18</sup> The characteristic matrix  $\mathbf{M}$  of a layer relates the electromagnetic fields at the two boundaries of the layer, that:

$$\begin{bmatrix} E_I \\ H_I \end{bmatrix} = \mathbf{M} \begin{bmatrix} E_{II} \\ H_{II} \end{bmatrix},$$

where  $E, H$  are the electric and magnetic fields, I and II refer to the beam incoming and outgoing boundaries, respectively (Fig. S1). Solving the boundary conditions of electromagnetic fields for TE waves, there is,

$$\begin{bmatrix} 1+r \\ (1-r)\tilde{n}_{\text{in}}\theta_{\text{in}} \end{bmatrix} = \mathbf{M} \begin{bmatrix} t \\ t\tilde{n}_{\text{out}}\theta_{\text{out}} \end{bmatrix},$$

with  $r$  being the reflection coefficient at boundary I, and  $t$  the transmission coefficient at boundary II. Therefore, both  $r$  and  $t$  can be calculated by knowing  $\mathbf{M}$ . Again for TE waves, we have:

$$\mathbf{M} = \begin{pmatrix} \cos \delta & \frac{i}{\tilde{n} \cos \theta} \sin \delta \\ i\tilde{n} \cos \theta \sin \delta & \cos \delta \end{pmatrix}$$

where  $\tilde{n}$  is the refractive index of the layer,  $\theta$  the refraction angle of the beam, and  $\delta = \tilde{n}kd \cos \theta$ , with  $k, d$  being the light wavevector and layer thickness, respectively.

For a system composed of  $m$  layers, there is:

$$\begin{bmatrix} 1+r \\ (1-r)\tilde{n}_{\text{in}}\theta_{\text{in}} \end{bmatrix} = \mathbf{M}_1 \mathbf{M}_2 \cdots \mathbf{M}_m \begin{bmatrix} t \\ t\tilde{n}_{\text{out}}\theta_{\text{out}} \end{bmatrix},$$

where  $r$  and  $t$  being the reflection and transmission coefficients of the multilayer system.

### 3. The infrared focal spot:

For the incident infrared beam, we assumed a Gaussian field distribution across the focal spot, that is:

$$E_{IR}(x, \lambda) = E_{IR0} \exp\left(-\frac{x^2}{w(\lambda)^2}\right)$$

with the  $x$ -axis being indicated in Fig. 1d, and  $w(\lambda)$  increasing with the infrared wavelength  $\lambda$ . For the system illustrated in Fig. 1d, the fraction of infrared light illuminating the VO<sub>2</sub> microbeam is:

$$f(\lambda) = \int_{-\Delta/2}^{\Delta/2} \exp\left(-\frac{x^2}{w(\lambda)^2}\right) dx \Bigg/ \int_{-\infty}^{\infty} \exp\left(-\frac{x^2}{w(\lambda)^2}\right) dx$$

where  $\Delta$  equals the width of VO<sub>2</sub>, and  $1-f(\lambda)$  is the fraction of infrared light illuminating the adjacent substrate. We obtained the overall reflectivity by summing up the reflection coefficient from VO<sub>2</sub> microbeam and adjacent substrate weighed by  $f(\lambda)$  and  $1-f(\lambda)$ , respectively.

#### 4. The temperature dependence of VO<sub>2</sub> absorption coefficient:

We could derive the VO<sub>2</sub> absorption coefficient at different temperatures from the infrared spectra in Fig. 2a. For the structure in Fig. 1d, the total reflectivity includes that from the top surface of VO<sub>2</sub> and that from all interfaces underneath (Fig. S-2a), which gives:

$$R(\omega) = \left| \tilde{r}_t(\omega) + \tilde{r}_b(\omega) \right|^2,$$

with  $\tilde{r}(\omega) = |\tilde{r}(\omega)|e^{i\phi(\omega)} = r(\omega)e^{i\phi(\omega)}$  being the reflection coefficient. For the  $i^{\text{th}}$  interference fringe centered at  $\omega_i$ , we define its contrast to be the difference between the maximum and minimum reflectivity reached at  $\omega_i \pm \Delta\omega/2$  (Fig. S-2b), hence we have:

$$\begin{aligned} \Delta R(\omega_i) &= R(\omega_i + \Delta\omega/2) - R(\omega_i - \Delta\omega/2) \\ &= \left| \tilde{r}_t(\omega_i + \Delta\omega/2) + \tilde{r}_b(\omega_i + \Delta\omega/2) \right|^2 - \left| \tilde{r}_t(\omega_i - \Delta\omega/2) + \tilde{r}_b(\omega_i - \Delta\omega/2) \right|^2, \quad (\text{S-1}) \\ &= \left[ r_t(\omega_i + \Delta\omega/2) + r_b(\omega_i + \Delta\omega/2) \right]^2 - \left[ r_t(\omega_i - \Delta\omega/2) + r_b(\omega_i - \Delta\omega/2) \right]^2 \end{aligned}$$

as a local maximum/minimum value of the reflectivity is achieved when  $\tilde{r}_t$  and  $\tilde{r}_b$  are in/out-of phase with each other. In the range of  $\sim 4000\text{-}6000\text{ cm}^{-1}$ , we found  $r_b \ll r_t$ , and  $r_t$  is nearly independent of  $\omega$  (Fig. S-2c), so Eq. (S-1) can be rewritten as:

$$\begin{aligned} \Delta R(\omega_i) \\ \approx 2r_t[r_b(\omega_i + \Delta\omega/2) + r_b(\omega_i - \Delta\omega/2)] + [r_b^2(\omega_i + \Delta\omega/2) - r_b^2(\omega_i - \Delta\omega/2)], \end{aligned} \quad (\text{S-2})$$

by expanding  $r_b$  with respect to  $\omega$ , we then have:

$$\Delta R(\omega_i) \approx 4r_t r_b(\omega_i). \quad (\text{S-3})$$

Since both  $\Delta R(\omega_i)$  and  $\tilde{n}(\omega_i)$  are single-valued functions of  $\omega_i$  in the range of  $\sim 4000\text{-}6000\text{ cm}^{-1}$ , Eq. (S-3) can be rewritten as  $\Delta R(\omega_i) \approx 4r_t r_b[\tilde{n}(\omega_i)]$ . In this frequency range,  $n$ , the real part of  $\tilde{n}$ , is nearly a constant<sup>17</sup>. Since the period of interference fringes remained the same upon heating,  $n$  is also insensitive to the temperature. Therefore, the frequency and temperature dependence of  $\tilde{n}$  is mainly from its imaginary part  $\kappa$ , hence the absorption coefficient  $\alpha = 2\omega\kappa/c$ . From Eq. (S-3), we then have  $\alpha$  being a single-valued function of the fringe contrast  $\Delta R$ :

$$\alpha(\omega_i, T) = \Im[\Delta R(\omega_i, T)]. \quad (\text{S-4})$$

In our analysis, we first found an interpolated function of  $\alpha(\omega_i)$  in the I-phase<sup>17</sup> with respect to  $\Delta R(\omega_i, T = 55^\circ\text{C})$ , then used this function to obtain  $\alpha(\omega_i, T)$  at elevated temperatures from  $\Delta R(\omega_i, T)$ , which are plotted in Fig. S-2(d).

## REFERENCES

- (S1) See, for example, Spizer, W. G. and Kleinman, D. A. *Phys. Rev.* **1961**, *121*, 1324.
- (S2) Wooten, F. *Optical Properties of Solids*, P. 53, Academic Press Inc., New York, 1972.
- (S3) Palk, E. D. *Handbook of Optical Constants of Solids*, Elsevier, 1998.

## FIGURE CAPTIONS

**FIGURE S-1.** Parameters used in the characteristic matrix calculation for a layered system.

**FIGURE S-2.** (a) and (b): Definitions of different quantities involved in the calculation. (a) Calculated spectra of  $R$ ,  $r_t^2$ , and  $r_b^2$ . (d) The measured fringe contrast versus frequency.

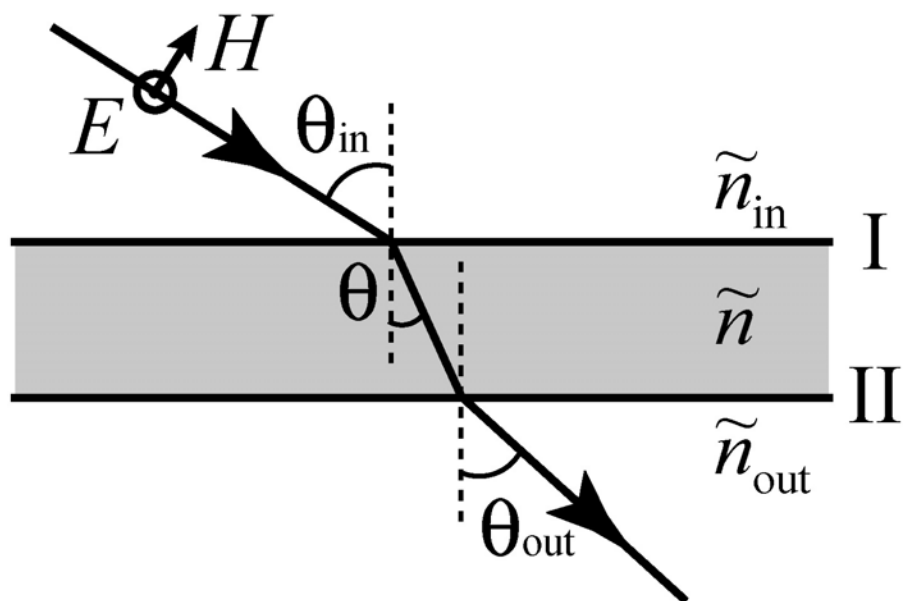


FIGURE S-1



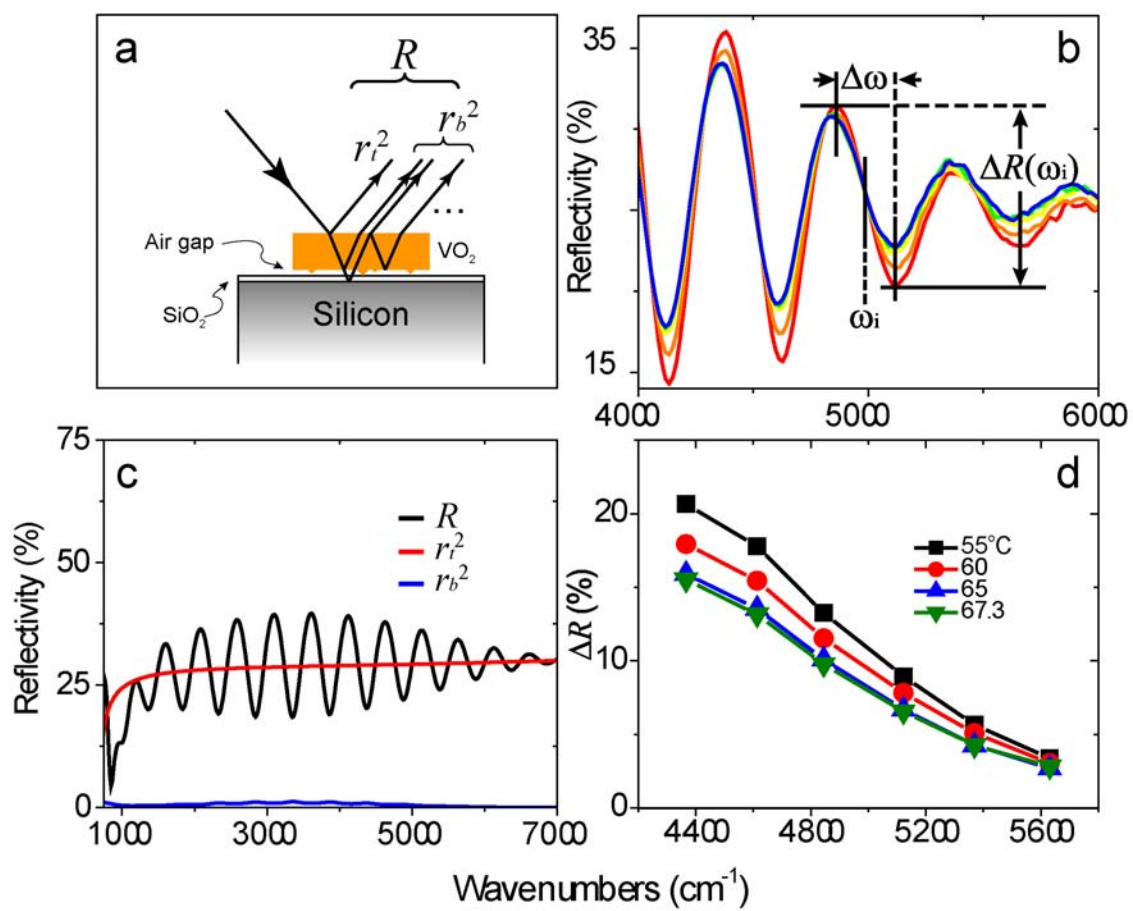


FIGURE S-2